ROYAL SOCIETY OF CHEMISTRY

PAPER

Check for updates

CeNiO₃ perovskite nanoparticles synthesized using gelatin as a chelating agent for CO₂ dry reforming of methane†

Usman Zahid,[a] Wahid Sidik Sarifuddin,[a] Abdul Hanif Mahadi,[a] Holilah,[b] Didik Prasetyoko [ID][c] and Hasliza Bahruji [ID] *[a]

CeNiO₃ perovskite nanoparticles were synthesized using gelatin as a chelating agent to catalyze the CO₂ dry reforming reaction. The optimization of gelatin concentration affects the formation of Ni coordinated on the B-sites of CeNiO₃. CeNiO₃ shows catalytic stability for 60 h with ∼50% CO₂/CH₄ conversion and a H₂/CO ratio of ∼0.8 when obtained using low concentrations of gelatin (0.05 g, 0.1 g). The exsolution of Ni nanoparticles from CeNiO₃ structures occurs during reduction treatment, expanding the crystal lattices of CeO₂. A high gelatin concentration (0.2 g) reduced Ni mobility and restricted Ni–Ce contacts. The uncoordinated Ni in CeNiO₃ exposes a high surface area (10.12 m² g⁻¹) for CH₄ dissociation, consequently increasing the H₂/CO ratio to ∼1.5 with 78% CH₄ and 53% CO₂ conversion. *In situ* DRIFTS analysis showed that CH₄ readily dissociates in the absence of CO₂, but CO₂ completes the reaction cycles by removing the carbon as CO gas.
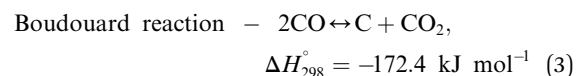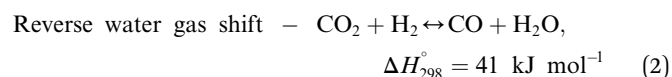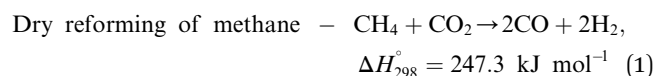
Sustainability spotlight

The exponential rise in energy demand is responsible for the depletion of natural fossil fuels and the rapid increase in Earth's temperature. The capture and utilization of CO₂ pave the way for a carbon-free industry. Dry reforming of methane (DRM) efficiently uses two greenhouse gases, carbon dioxide and methane, to produce synthesis gas (CO + H₂) as feedstock in the Fischer–Tropsch reaction. This study aims to utilize gelatin as a chelating agent for synthesizing CeNiO₃ perovskite to enhance stability for CO₂ dry reforming. The H₂/CO ratio relies on Ni coordination that can be controlled by variations in gelatin concentration. We emphasize the route to achieve SDG 7 (affordable and clean energy) and SDG 13 (climate action) of the UN sustainable development goals.

Introduction

The exponential rise of fossil fuel usage to sustain global energy demand is responsible for the depletion of natural fossil fuels and the rapid increase in CO₂ levels in the atmosphere.[1] The Paris Agreement of 2015 aimed to reduce greenhouse gas emissions to limit global temperature rise to 1.5 °C.[2,3] The agreement encouraged the energy sector to adopt more sustainable and greener sources,[4] paving a path for carbon-neutral energy. Dry reforming of methane (DRM) uses two greenhouse gases, carbon dioxide and methane, to produce synthesis gas (CO + H₂) as feedstock in the Fischer–Tropsch reaction.[5] The ideal H₂/CO ratio is one, but side reactions such

as reverse water gas shift (RWGS) and Boudouard reactions cause variations in the H₂/CO ratio.[6]

Dry reforming of methane −
$$CH_4 + CO_2 \rightarrow 2CO + 2H_2,$$
$$\Delta H_{298}^{\circ} = 247.3 \text{ kJ mol}^{-1} \quad (1)$$

Reverse water gas shift −
$$CO_2 + H_2 \leftrightarrow CO + H_2O,$$
$$\Delta H_{298}^{\circ} = 41 \text{ kJ mol}^{-1} \quad (2)$$

Boudouard reaction −
$$2CO \leftrightarrow C + CO_2,$$
$$\Delta H_{298}^{\circ} = -172.4 \text{ kJ mol}^{-1} \quad (3)$$

The main challenge in dry reforming is the highly endothermic reaction for co-activation of the C–O bond in CO₂ and the C–H bond in CH₄. Due to thermodynamic constraints, many developments have been made for high-temperature DRM (>700 °C),[7] causing thermal degradation of catalysts and carbon deposition.[8,9] Designing stable catalysts with carbon-resistant properties can enhance catalyst stability.[10] Metal oxides with stable structures, such as pyrochlore, perovskites, and mixed oxides, have been employed to improve structural stability.[11] Ce-based catalysts exhibited high performance in DRM due to the

[a]Center for Advance Material and Energy Science, Universiti Brunei Darussalam, Jalan Tungku Link, Brunei Darussalam. E-mail: hasliza.bahruji@ubd.edu.bn

[b]Research Center for Biomass and Bioproducts, National Research and Innovation Agency of Indonesia (BRIN), Cibinong, Indonesia

[c]Department of Chemistry, Faculty of Sciences, Institut Teknologi Sepuluh Nopember, Keputih Sukolilo, Surabaya, 60111, Indonesia

† Electronic supplementary information (ESI) available. See DOI: https://doi.org/10.1039/d4su00268g

oxygen mobility in ceria that inhibits carbon deposition.[12] The general formula of ABO_3 perovskite consists of metallic cations with different ionic radii occupying the A and B sites of the cubic structure, with the small metal occupying the B site. Under a reducing environment such as in dry reforming reactions, Ni on the B-sites of $CeNiO_3$ perovskite exsolves to form highly dispersed Ni nanoparticles.[13] The multivalency of perovskite from rare earth elements offers excellent redox properties and oxygen vacancies. Perovskite comprises 60% oxygen atoms that can facilitate carbon gasification.[14]

The synthesis of $CeNiO_3$ that requires high calcination temperatures up to 800 °C produced low surface area perovskites. $CeNiO_3$ produced using auto-combustion of glycine and metallic nitrate precursors showed CO_2 conversion reduced from 65% to 55% in 7 h at 700 °C.[12,15] High surface area perovskites were synthesized by modification of sol–gel synthesis with an organic template that can reach 30–40 m^2 g^{-1}.[16] Nanocasting methods with hard templates such as SBA-15 and MCM-41 increased the surface area to 100 m^2 g^{-1}.[17] Since most catalytic applications of perovskite for dry reforming of methane rely on the exsolution of isolated Ni nanoparticles, having a high surface area $CeNiO_3$ will enhance Ni dispersion and reduce the nanoparticle size. Most studies focused on partially substituting $CeNiO_3$ perovskite with other metals such as Zr and Y to enhance lattice oxygen capacity.[18] $CeNiO_3$ substituted with La produced using citric acid as a chelating agent reduced Ni aggregation to enhance catalytic stability.[19]

Employing a chelating agent in the synthesis mixtures formed a stable and uniform gel between the metal precursors.[20] The optimization of chelating agents stabilized the octahedral Ni bonds for transformation into stable ionic structures. In dry reforming of methane, the reaction under a continuous reducing environment exsolves Ni to form highly dispersed nanoparticles. Metal exsolution in perovskites is initialized from the surfaces and/or grain boundaries,[21] which are enriched with oxygen vacancies and A-site deficiencies.[22] Despite the multitude of benefits of $CeNiO_3$, the agglomerated crystals reduce the available surface for Ni exsolution. Gelatin has been utilized as an organic template and chelating agent for metal ions for synthesizing porous materials. As a chelating agent, gelatin forms a strong bond with metals *via* interaction with the amino and carbonyl groups.[23] The stable hydrophilic colloid protects the sol during sol–gel synthesis, controlling the growth of nanoparticles.[24] The chelating ability of gelatin arises from the combination of high molecular weight protein and amine and carboxyl group functionality. Therefore, this study aims to investigate the effect of gelatin as a chelating agent on the catalytic performance of $CeNiO_3$ perovskites in a dry reforming reaction. The correlation between crystal structures and catalytic properties was observed upon variation in gelatin concentration.

Results and discussion

XRD analysis

The XRD analysis of as-synthesized $CeNiO_3$ perovskite with different concentrations of gelatin was conducted on the
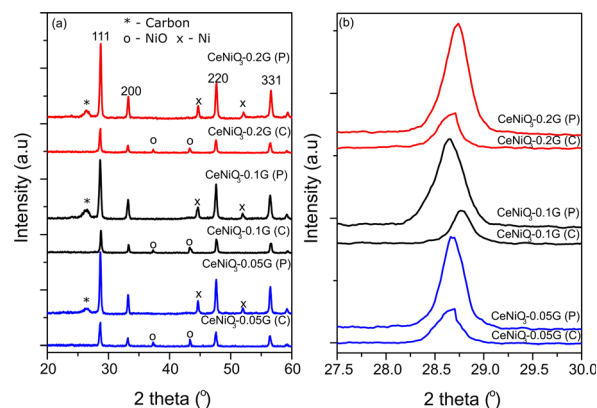

Fig. 1 XRD of $CeNiO_3$ perovskite with (a) different concentrations of gelatin after calcination (C) and after the reaction (P); (b) changes in the high intense diffraction peak with different concentrations of gelatin before and after the reaction.

catalysts after calcination at 900 °C and after a 24 h dry reforming reaction at 600 °C (Fig. 1a). The peaks at $2\theta = 28.7°$, 33.3°, 37.3°, 43.3°, 47.7°, and 56.5° confirm the formation of a crystalline $CeNiO_3$ perovskite structure.[12,25–27] The diffraction peaks of the cubic phase NiO can be observed at $2\theta = 37.3°$ and 43.3°. Close observation of the range $2\theta = 27.5–30°$ reveals the shift of the (111) peak from 28.6° at 0.05 g of gelatin to 28.7° at 0.1 g of gelatin (Fig. 1b). However, increasing gelatin to 0.2 g shifted the (111) peak to $2\theta = 28.6°$. The calculated unit cell parameters in Table 1 further indicate the reduction of lattice parameters from 5.389 Å to 5.379 Å with increasing gelatin concentration from 0.05 g to 0.1 g. The lattice contraction of the CeO_2 (111) plane implies a different degree of Ni incorporation in the B-site of perovskite.

The variation in contraction of CeO_2 lattice spacing suggests that the inclusion of Ni in the $CeNiO_3$ perovskite structure relies on gelatin concentration. There is also a possibility of the formation of a $CeNiO_3 + CeO_2 + NiO$ mixture. However, such formation is difficult to prove by XRD analysis. Nevertheless, the shift of the CeO_2 peak to high 2θ, while the NiO peak remains at similar $2\theta = 37.3°$ and 43.3°, suggests the inclusion of Ni in the CeO_2 lattice, forming $CeNiO_3$ perovskite.

XRD analysis of $CeNiO_3$ after 24 h of dry reforming of methane (DRM) shows the absence of the NiO peak due to reduction to Ni metal at $2\theta = 44.5°$ and 52.1°. By comparing the XRD of synthesized $CeNiO_3$-0.05G and after the DRM reaction, there is a slight shift of the (111) peak toward a lower angle, as shown in Fig. 1b. The shift is more apparent in $CeNiO_3$-0.1G. The exsolution of NiO to the surface of CeO_2 under reduction causes Ni nanoparticle formation and CeO_2 lattice expansion. However, for $CeNiO_3$-0.2G, the (111) peaks do not shift to a lower 2θ, which might indicate that NiO formed as nanoparticles deposited on CeO_2, rather than $CeNiO_3$. A new peak also appeared at $2\theta = 26.2°$, which shows carbon formation on the catalysts after a 24 h reaction (Fig. 1).

Table 1 summarizes the crystallite size, unit cell parameters (a), and volume of $CeNiO_3$ catalysts before and after a 24 h catalytic reaction. The crystallite sizes of $CeNiO_3$ perovskites

Table 1 Crystallite size and unit cell parameters of CeNiO$_3$ perovskites with different concentrations of gelatin[a]
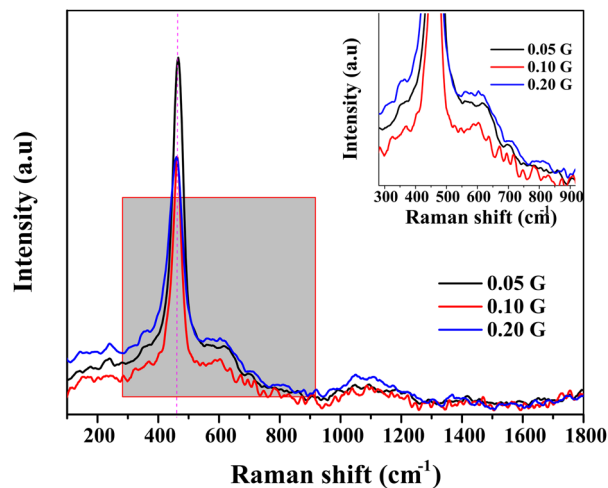
Amount of gelatin	D (nm)	a (Å)	V (Å^3)
0.05 g (C)	29	5.389	156.581
0.05 g (P)	29	5.397	157.224
0.10 g (C)	34	5.379	155.624
0.10 g (P)	24	5.401	157.546
0.20 g (C)	32	5.388	156.421
0.20 g (P)	28	5.383	155.942

[a] C: calcined; P: post-reaction.

Fig. 2 Raman spectra of CeNiO$_3$ perovskite with varied concentrations of gelatin.

synthesized at different gelatin concentrations are quite similar at approximately ~29–34 nm. The unit cell parameters of CeNiO$_3$ synthesized using different gelatin concentrations were determined to understand the incorporation of Ni in B sites. At 0.05 g of gelatin, CeNiO$_3$ exhibited a unit cell parameter of 5.389 Å, slightly larger than that of CeNiO$_3$ obtained using 0.1 g gelatin at 5.379 Å. However, CeNiO$_3$ obtained using 0.2 g gelatin showed a unit cell parameter of 5.388 Å. The decrease in unit cell parameters indicates the incorporation of Ni^{2+}, which has a smaller ionic radius, into CeO$_2$.[28] Using 0.1 g gelatin enhanced Ni incorporation into CeNiO$_3$ perovskite, causing significant lattice contraction. High lattice strain in perovskite implies a weak metal–oxygen bond in BO$_6$ octahedra, which is susceptible to oxygen vacancy formation.[29] The increase of lattice volume (V) after a 24 h catalytic reaction suggested the expansion of the CeO$_2$ lattice following the exsolution of Ni nanoparticles. A high degree of lattice expansion was observed on CeNiO$_3$, obtained using 0.05 g and 0.1 g of gelatin, in which the lattice volume of CeNiO$_3$-0.05G enhanced by 0.4% and that of CeNiO$_3$-0.1G enhanced by 1.21% after a 24 h reaction. However, CeO$_2$-0.2G exhibited different behaviors, exhibiting lattice volume reduction by 0.03%. The observation implied that at high gelatin concentration, NiO was deposited as nanoparticles on CeO$_2$. Following long catalytic reduction under a reducing environment, Ni was doped onto CeO$_2$, causing lattice contraction.[30]

Raman analysis

Fig. 2 shows the recorded Raman spectra from 2000 cm^{-1} to 200 cm^{-1}. CeNiO$_3$ perovskite shows a highly intense peak at ~460 cm^{-1}, a characteristic peak of cubic fluorite structure CeO$_2$.[31] This sharp peak is related to the F$_{2g}$ symmetric stretching of oxygen atoms around the cerium ions.[32] The variation of gelatin concentrations from 0.05 g to 0.2 g reduced the intensity of the F$_{2g}$ peak. The peak also broadens and is red-shifted at 0.2 g gelatin concentration, implying a decrease in CeO$_2$ crystallite size. The strain due to the high curvature of nanoparticles and surface defects also red-shifted the peak.[33–35] A small peak at 225 cm^{-1} only appeared in ceria when doping with ionic metals with different ionic radii,[36] attributed to the second-order transverse acoustic (2TA) mode. The peaks at 595 cm^{-1} are ascribed to defect-induced (D) mode, presumably due to the presence of oxygen vacancies or cation substitution

in the lattices.[36,37] The oxygen vacancies produced at the redox site in ceria-based materials play a prime role in removing the deposited carbon during the dry reforming reaction. The ratio between the intensity of defect induced (D) mode and the strong F$_{2g}$ mode ($I_D/I_{F_{2g}}$) can be used for the estimation of oxygen vacancies in ceria-based catalysts.[38,39] The concentration of oxygen vacancies in CeNiO$_3$ synthesized using 0.05 g, 0.1 g and 0.2 g gelatin was 0.85, 0.88 and 0.90, respectively (Table 2).

Temperature programmed reduction (TPR)

Temperature programmed reduction (TPR) examines the metal–support interaction and reducibility of the catalysts. Fig. 3 shows the TPR profiles of CeNiO$_3$ perovskite synthesized at different concentrations of gelatin. Three reduction peaks appeared for the TPR profile of CeNiO$_3$ synthesized using 0.05 g of gelatin. The broad reduction peaks at 393 °C correspond to Ni^{2+} to Ni^0 reduction.[12] A small peak at 530 °C was due to the reduction of surface ceria, while a high temperature reduction peak at 802 °C corresponds to the reduction of bulk oxygen in ceria.[40] CeNiO$_3$ perovskite synthesized using 0.1 g of gelatin shows similar TPR profiles to CeNiO$_3$ (0.05 g). However, for CeNiO$_3$ synthesized with 0.2 g gelatin, the reduction peaks of NiO shift to 435 °C with a small shoulder peak at 395 °C. The reduction peak for surface CeO$_2$ also shifts to 545 °C, while the peak ascribed to the reducibility of lattice oxygen species appeared to shift to 833 °C. Increasing gelatin concentration resulted in enhanced interfacial interaction between NiO and CeO$_2$ based on the high temperature reduction. CeNiO$_3$ with 0.05 g and 0.10 g gelatin also shows similar reduction peaks and hydrogen consumption at ~44 mmol g$_{cat}$$^{-1}$ while 0.20 g of gelatin shows a slight enhancement to 55 mmol g$_{cat}$$^{-1}$ (Table 2). The higher hydrogen consumption implies a high oxidation ability of CeNiO$_3$-0.2G. CO chemisorption on reduced CeNiO$_3$ provides information on Ni dispersion and the surface area. The results suggest that increasing gelatin concentration to 0.2 g significantly enhanced Ni dispersion by 1.52% and the Ni

Table 2 Physicochemical properties of $CeNiO_3$ perovskites synthesized using different concentrations of gelatin

Catalysts	$I_D/I_{F_{2g}}$[a]	Temp (°C)			H_2[b] (mmol g_{cat}^{-1})	Ni dispersion[c] (%), (µmol g^{-1})	Ni surface area[c] ($m^2 g^{-1}$)	CO_2 emission[d] (mmol g_{cat}^{-1})	Carbon[e] (%)
		P1	P2	P3					
$CeNiO_3$ 0.05G	0.85	393	531	802	44.48	0.58, 19.64	3.84	1.54	58.8
$CeNiO_3$ 0.10G	0.88	394	534	805	44.79	0.24, 8.01	1.57	1.43	56.7
$CeNiO_3$ 0.20G	0.90	435	545	833	55.08	1.52, 51.76	10.12	0.90	42.4

[a] Calculated from Raman spectroscopy. [b] Calculated from H_2-TPR analysis. [c] Calculated from CO chemisorption. [d] Calculated from TPO analysis. [e] Calculated from CHNS–O analysis.
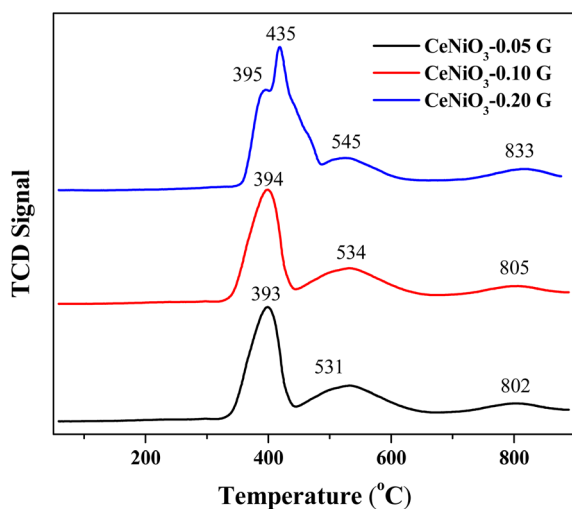

Fig. 3 H_2-TPR profiles of $CeNiO_3$ perovskites obtained using different concentrations of gelatin.

from 0.05 g to 0.2 g. The results were further supported by CHNS–O analysis, which is summarized in Table 2.

N₂ adsorption/desorption analysis

The textural properties of $CeNiO_3$ perovskite were analyzed using N_2 adsorption–desorption analysis (ESI, Fig. S2†). According to the IUPAC porosity classification, $CeNiO_3$ perovskites synthesized using 0.05 g and 0.1 g gelatin show type IV isotherms,[45] indicating the formation of mesoporous structures. The isotherm also exhibits a hysteresis loop H_3 due to the capillary condensation occurring in mesoporous structures. However, $CeNiO_3$ obtained using 0.2 g gelatin shows a very slow nitrogen uptake up to $P/P_o = 0.9$, resembling a type III nonporous material. All the catalysts show strong adsorption at high relative pressure, indicating the presence of large pores. Large pores are beneficial for the diffusion of adsorbate gas. There is a trend in the surface area with adding more gelatin. $CeNiO_3$ perovskite with 0.05 g concentration of gelatin has a surface area of 17.65 $m^2 g^{-1}$. At 0.1 g of gelatin, the surface area reduced

surface area by 10.12 $m^2 g^{-1}$. There is a possibility that at high gelatin concentration, some of the NiO were not incorporated into the $CeNiO_3$ perovskite lattice but were instead impregnated on the surface of CeO_2 as nanoparticles, as implied by XRD analysis.

Temperature programmed oxidation

Temperature programmed oxidation (TPO) has been performed to determine the carbonaceous species on 24 h post-reaction catalysts. The TPO profiles of the fresh $CeNiO_3$ catalyst show negligible oxidation up to 800 °C (ESI, Fig. S1†). The TPO profiles of all spent catalysts confirm that the oxidation of graphitic carbon occurred at 600–700 °C (Fig. 4).[41,42] No peak was associated with the amorphous carbon oxidation at 250–400 °C,[43] suggesting efficient oxidation of amorphous carbon to CO during the reaction. As indicated by Raman analysis, oxygen vacancies facilitate the oxidation of carbonaceous species.[44] However, since the reaction was performed at 600 °C, the temperature is too low to oxidize graphitic carbon. The intensity of the oxidation peak at ~600 °C decreases when using $CeNiO_3$ synthesized using a high concentration of gelatin. CO_2 emissions were reduced from 1.54 mmol g_{cat}^{-1} to 0.90 mmol g_{cat}^{-1} when using $CeNiO_3$ with the gelatin concentration increasing
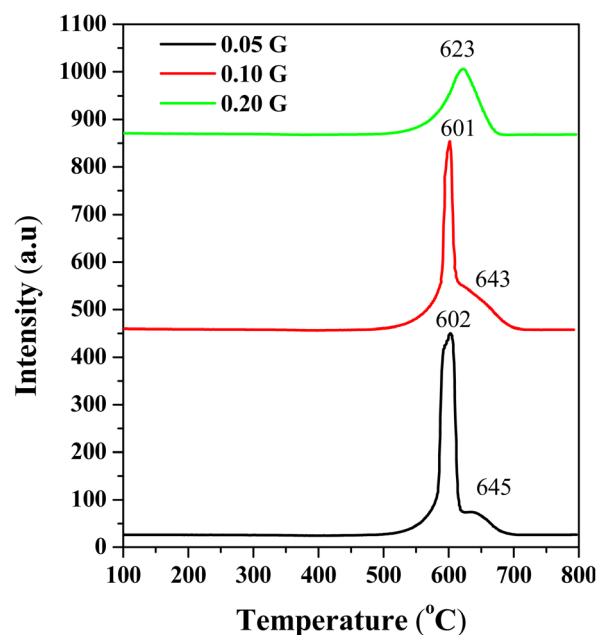

Fig. 4 TPO profiles of substituted $CeNiO_3$ perovskites synthesized using different concentrations of gelatin after a 24 h dry reforming reaction at 600 °C.

Table 3 Textural properties of CeNiO₃ perovskites

Catalysts	BET surface area (m² g⁻¹)	Pore volume (cm³ g⁻¹)	Pore diameter (nm)
CeNiO₃-0.05G calcined	17.65	0.055	10.4
Post-reaction	74.18	0.19	8.5
CeNiO₃-0.10G calcined	13.30	0.044	11.3
Post-reaction	58.72	0.18	9.98
CeNiO₃-0.20G calcined	11.48	0.072	21.05
Post-reaction	35.45	0.1	11.03

to 13.30 m^2 g^{-1}, while increasing the gelatin concentration to 0.20 g significantly reduced the surface area of CeNiO₃ to 11.48 m^2 g^{-1} (Table 3).

N₂ analysis was also conducted on the catalysts recovered from a 24 h dry reforming reaction at 600 °C. There is clear evidence of changes in the N₂ isotherm with a higher N₂ uptake compared to the fresh catalysts (ESI, Fig. S2†). All CeNiO₃ catalysts displayed a larger hysteresis loop at P/P_o = 0.4 to 0.9, indicating the formation of mesoporous structures. The surface area enhances to 35.45 m^2 g^{-1} for CeNiO₃-0.2G, 58.72 m^2 g^{-1} for CeNiO₃-0.1G and 74.18 m^2 g^{-1} for CeNiO₃-0.05G. The surface areas of CeNiO₃ catalysts were enhanced due to the formation of porous carbon as the by-product of carbon deposition on the catalysts during long catalytic reactions.

HR-TEM analysis

High resolution transmission electron microscopy (HR-TEM) was employed to study the morphology of CeNiO₃-0.1G after calcination and a 24 h DRM reaction at 600 °C (Fig. 5a). The average estimated particle size of calcined CeNiO₃ perovskite was 43.7 nm (Fig. 5g). The selected area electron diffraction pattern (SAED) shows (111), (200), (222), (400) and (220) lattice planes, which confirm the formation of CeNiO₃ perovskite (Fig. 5b). The HR-TEM image after 24 hours of the DRM reaction shows the exsolution of Ni from CeNiO₃ and the formation of carbon nanotubes (Fig. 5c). The estimated particle size of CeNiO₃ perovskite after DRM was 71.5 nm, slightly larger than the calcined catalysts due to particle sintering (Fig. 5h). The SAED pattern shows the enlargement of (220) and (111) lattice planes, implying CeO₂ phase formation after the reduction of CeNiO₃ perovskite (Fig. 5d). By comparing the TEM images of calcined and post-reaction CeNiO₃, Ni nanoparticles were observed as large nanoparticles at ∼8 nm and small nanoparticles at ∼1 nm (Fig. 5f). The results show non-uniform exsolution of Ni from CeNiO₃ after a 24 h reaction. Fig. 5e shows the formation of carbon nanotubes on post-reaction catalysts with a lattice diameter of 0.34 nm. The carbon nanotube diameter was estimated to be 45 nm. The carbon nanotube existed as crystalline carbon with no distinguishable amorphous carbon shell.

XPS analysis

Fig. 6 shows the XPS analysis of CeNiO₃-0.1G after calcination at 900 °C and after a 24 h dry reforming reaction at 600 °C. The Ni

2p spectra of calcined CeNiO₃ show peaks at 853.5 eV and 855.2 eV ascribed to Ni^{2+} of NiO and Ni^{3+} of Ni₂O₃.[46–48] Ni exists as NiO, occupying the B-sites of CeNiO₃ and the under-coordinated Ni defects. The uncoordinated Ni^{3+} species implies the presence of Ni^{2+} vacancies that may act as active sites for C–H dissociation. Post-reaction catalysts show binding energy shifts to 852.5 eV, implying NiO reduction to Ni metal after the dry reforming reaction.[49] The second Ni 2p peak shifted to a higher binding energy of ∼856.5 eV, presumably due to the formation of NiOOH species.[50] NiO was exsolved from the perovskite structure, forming Ni nanoparticles on CeO₂ surfaces. Following CH₄ decomposition, Ni was partially oxidized on the surface, forming NiO(OH) species. The changes in Ni 2p binding energy prove the changes in the Ni environment following 24 h of reactions.

The Ce 3d spectra confirm the presence of Ce^{3+} and Ce^{4+} in CeNiO₃ before and after the catalytic reaction. The deconvoluted peaks divided the spectra into five pairs of $3d_{5/2}$ and $3d_{3/2}$ spin–orbit components, representing the electronic transition between Ce^{4+} and Ce^{3+}. The high intensity peaks at 882.2 eV, 900.8 eV, 898.1 eV, and 916.2 eV and the medium intensity peaks at 888.8 eV and 906.9 eV are assigned to Ce^{4+}. The low intensity peaks at 885.5 eV and 903.9 eV are assigned to Ce^{3+} cations.[51] Increased concentrations of Ce^{3+} species are evident on the catalyst after a 24 h reaction. The ratios between Ce^{4+} and Ce^{3+} were determined based on the sums of the integrated peak areas of each species. The intensities of Ce^{3+} peaks increase relative to the Ce^{4+} peak after a prolonged catalytic reaction. The oxidation of adsorbed C species involves the mobility of oxygen on CeO₂. The transition of tetravalent Ce^{4+} to trivalent Ce^{3+} correlates with the formation of oxygen vacancies.[52] A detailed analysis of surface oxygen species was conducted based on O 1s spectra. The O 1s spectra revealed a peak at 529.2 eV due to lattice oxygen species. The peak at 531.0 eV is assigned to the surface hydroxyl group and is used to imply the presence of defective oxygen. The peak at 533.0 eV is ascribed to oxygen bonded to carbon species. An increase in surface oxygen vacancies was observed on the post-reaction catalysts based on the enhanced surface hydroxyl group peak at 531.0 eV. The composition of oxygen from the carbonyl compound (O–C) was also enhanced to 13.73%. The percentage of O 1s species tabulated in Table 4 shows the enhanced concentration of O–C and O–H. The shift to higher BE, ascribed to the less electron-rich oxygen species in the adsorbed state, represents the surface oxygen vacancies generated following Ni exsolution. The results are in agreement with the increased Ce^{3+} peaks after catalytic reactions. The reducibility of Ce^{4+} to Ce^{3+} is responsible for fast oxygen vacancy production and promotes carbon oxidation to CO.

The nature of the C 1s peak of the fresh and post-reaction catalysts provides information on the carbon deposition after the reaction. The first peak at 284.4 eV indicates the sp² C=C bond of graphite carbon.[53] Note that adventitious carbon appeared at 284.4 eV as the major C 1s peak on the fresh catalysts,[54] together with the C–C peak at 285.8 eV, the C=O peak at 287.5 eV and the C=O peak at 288.4 eV. The calcined samples were dominated by graphitic C=C carbon at 69%. Five carbon
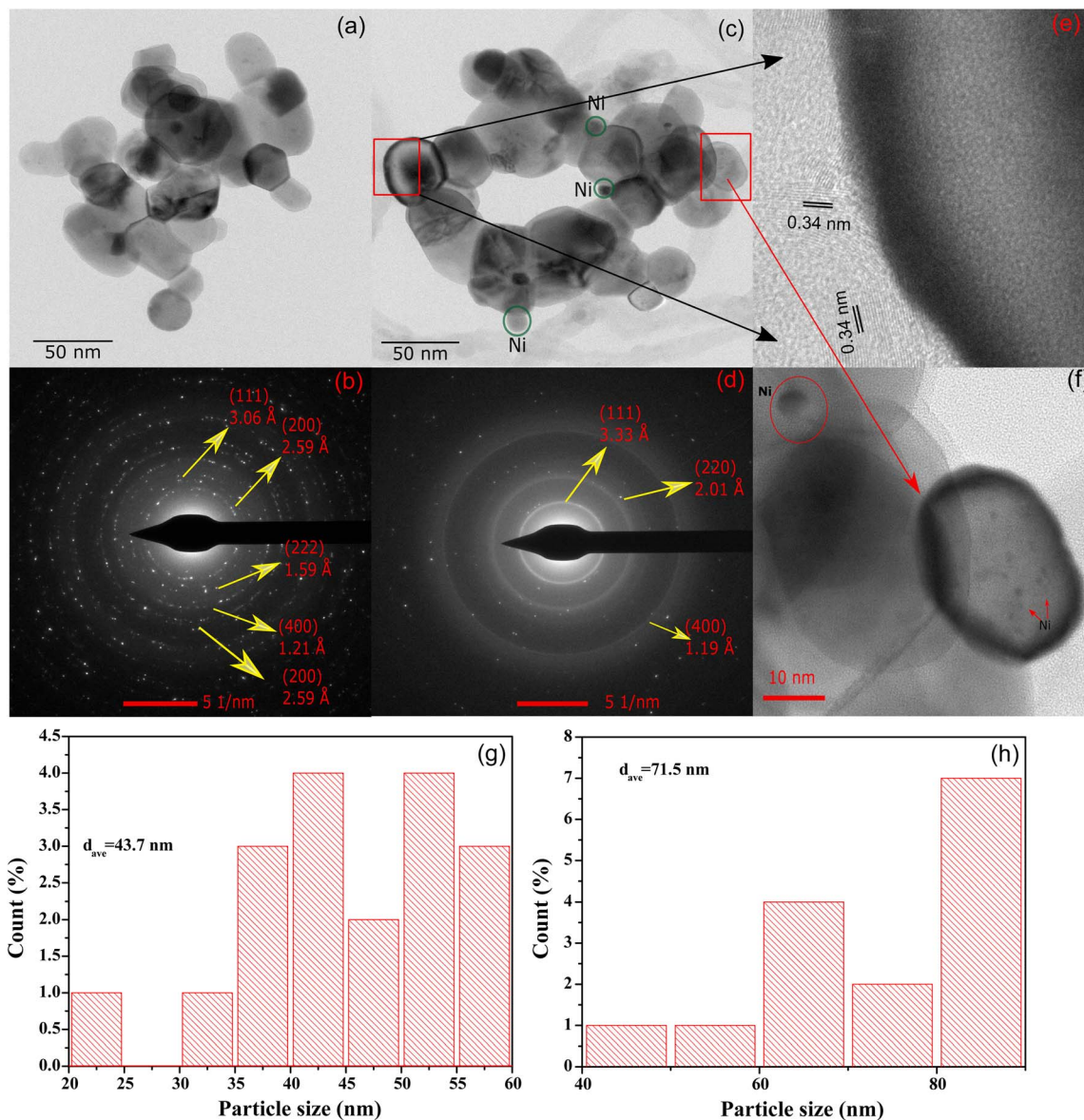
Fig. 5   HR-TEM images of (a) calcined CeNiO$_3$-0.1G perovskite; (b) SAED pattern; (c) HR-TEM images of CeNiO$_3$ after DRM; (d) SAED pattern; (e) carbon nanotube on post-reaction CeNiO$_3$; (f) Ni nanoparticles on CeO$_2$ after a 24 h reaction: (g) particle size distribution of CeNiO$_3$-0.1G after calcination; and (h) particle size distribution of CeNiO$_3$-0.1G after 24 h DRM reaction.

species were determined for the post-reaction catalyst, with an additional carboxyl or ester carbon COO– peak at 290.5 eV.[55] The peak at 284.4 eV is ascribed to the graphitic sp^2 C=C carbon nanotube as evidenced by HRTEM analysis. Another small peak at 285.8 eV indicates C–C and C–H hydrocarbon.[56] The third peak at 287.5 eV is assigned to the C–O bond, while the peak at 288.4 eV is assigned to the C=O bond.[57] It appears that graphite C–C carbon is the main composition with 76% concentration.

Catalytic performance

All CeNiO$_3$ perovskites were reduced *in situ* before the reaction using 20 mL min^{-1} of hydrogen at 500 °C for 3 hours. Catalytic activity was investigated for a long-term reaction at 600 °C for 24 hours (Fig. 7). CeNiO$_3$-0.05G displayed stable CH$_4$ conversion at

50% throughout the 24 h catalytic reaction (Fig. 7a). Approximately similar CO$_2$ conversion was observed at 48%, although the catalysts experienced an induction period within three hours of the reaction. CeNiO$_3$ underwent exsolution to form Ni/CeO$_2$ under hydrogen pre-treatment. The induction period during the catalytic reaction might suggest that the exsolution of Ni nanoparticles continuously occurred following the introduction of CH$_4$/CO$_2$ mixtures until they reached a steady state. The generation of oxygen vacancies from the Ce^{4+}/Ce^{3+} transition enhanced CO$_2$ adsorption and reduction to carbon monoxide. Consequently, the H$_2$/CO ratios were gradually reduced to reach 0.85 at 24 h of reaction (Fig. 7d). A 60 h stability test was performed on CeNiO$_3$ perovskite synthesized using 0.1 g of gelatin. The CeNiO$_3$ showed a higher CH$_4$
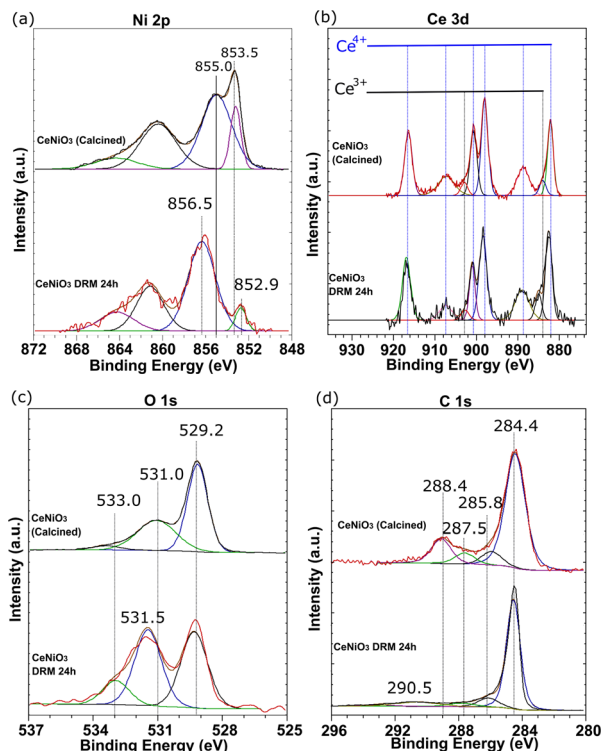
Fig. 6 XPS analysis of (a) Ni 2p, (b) Ce 3d, (c) O 1s, and (d) C 1s of CeNiO$_3$ (0.1 g gelatin) after calcination at 900 °C and the catalyst recovered from 24 h dry reforming at 600 °C.

Fig. 7 Catalytic activity for a 24 h dry reforming reaction at 600 °C using CeNiO$_3$ perovskite: CH$_4$ and CO$_2$ conversion using (a) CeNiO$_3$-0.05 G catalyst; (b) CeNiO$_3$-0.1G catalyst; (c) CeNiO$_3$-0.2G catalyst; and (d) H$_2$/CO ratios.

conversion than CO$_2$ within five hours of the reaction (Fig. 7b). The CH$_4$ conversion was gradually reduced to reach approximately similar CO$_2$ conversion of 52%. The H$_2$/CO ratio was initially high at ~0.95 and then continued to decrease with time, reaching stability at 0.87 between 9 and 60 hours of the reaction. In contrast, the CO$_2$ and CH$_4$ conversion of CeNiO$_3$ synthesized using 0.2 g of gelatin is stable for 24 h at 74% and 51%, respectively (Fig. 7c). Due to a higher conversion of CH$_4$ than CO$_2$, the ratio of H$_2$/CO exceeds 1.0, reaching ~1.6 throughout the 24 h reaction.

The deviation of the H$_2$/CO ratio from stoichiometry is due to side reaction reactions that take place, such as reverse water gas shift reaction (RWGS) (eqn (2)) and Boudouard reaction (eqn (3)). In CeNiO$_3$ synthesized using 0.05 g and 0.1 g gelatin, the low H$_2$/CO < 1 may be due to the reaction of hydrogen with CO$_2$ via a reverse water gas shift reaction. This step further enhances CO production, thus causing less hydrogen yield
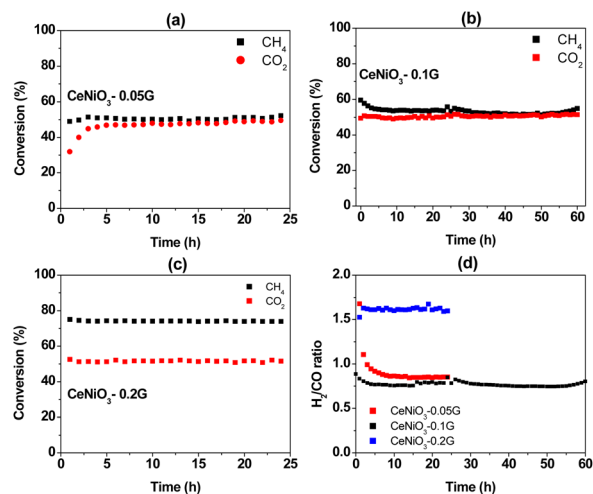
despite achieving approximately similar CO$_2$ and CH$_4$ conversion. However, for CeNiO$_3$ obtained using 0.2 g gelatin, a high surface area of Ni caused the fast decomposition of CH$_4$ into hydrogen gas. Interestingly, the catalysts were highly stable despite the formation of graphitic carbon, as evidenced by XRD, TEM, and TPR analysis. Based on N$_2$ adsorption and TEM analysis, the graphitic carbon was identified as a highly porous carbon nanotube. Therefore, there is a possibility that the porous carbon allows diffusion of CO$_2$/CH$_4$ gases to reach active sites, thus preventing deactivation.

Based on the difference in the catalytic performance of CeNiO$_3$ perovskite with 0.05 g and 0.20 g of gelatin, the catalysts were investigated at different reaction temperatures. The performance of CeNiO$_3$ perovskite was studied at 400–600 °C under a constant flow of 20 mL min^{-1} mixed CO$_2$/CH$_4$/N$_2$ gases. Fig. 8(a–c) shows the plot of methane conversion, carbon dioxide conversion and the H$_2$/CO ratio at different temperatures. Initially, carbon dioxide conversion, methane conversion, and the H$_2$/CO ratio are low at 400 °C with less than 10% conversion. However, CeNiO$_3$ synthesized using 0.2 g gelatin concentration exhibited 9.22% CH$_4$ conversion and 10.04% CO$_2$ conversion to give 1.26 H$_2$/CO ratios. The catalytic performance was slightly higher than that of CeNiO$_3$ obtained at lower gelatin concentrations. There was an exponential rise in CH$_4$ and CO$_2$ conversion with increased temperatures. The highest

Table 4 XPS analysis of CeNiO$_3$-0.1G after calcination and 24 h dry reforming of methane at 600 °C; the [Ce^{4+}]/[Ce^{3+}] atomic ratio, the binding energy (eV) for the C 1s components, and the O 1s surface composition

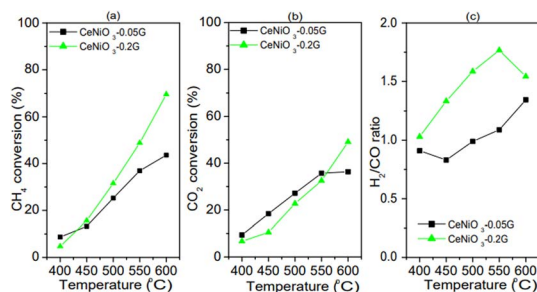| Cat.	[Ce^{4+}]/[Ce^{3+}]	C 1s percentage (atom%)					O 1s percentage (atom%)		
		C=C (284.8 eV)	C–C (285.8 eV)	C–O (287.5 eV)	C=O (288.4 eV)	COO– (290.5 eV)	O$_I$ (529.1 eV)	O$_{OH}$ (531.03 eV)	O$_{oc}$ (533.31)
Calcined	14.41	69.52	8.34	6.98	15.17	—	57.73	38.01	4.19
Post-reaction	10.86	79.99	10.20	5.17	2.23	2.27	43.15	43.12	13.73

Fig. 8 Catalytic performance of $CeNiO_3$ perovskites at different temperatures: (a) CH_4 conversion; (b) CO_2 conversion; and (c) H_2/CO ratios from $CeNiO_3$-0.05G, $CeNiO_3$-0.1G and $CeNiO_3$-0.2G.

69.62% CH_4 conversion with 49.05% carbon dioxide conversion was obtained on $CeNiO_3$(0.20) to give a H_2/CO ratio of 1.54. $CeNiO_3$ synthesized at 0.2 g gelatin concentration shows a higher catalytic conversion to CH_4 than CO_2, resulting in a higher H_2/CO ratio.

In situ DRIFTS analysis

In situ DRIFTS analysis was performed to investigate intermediate species in the DRM reaction at different temperatures (Fig. 9). The catalyst was reduced with hydrogen under a constant flow of 20 mL min^{-1} at 500 °C before the DRM reaction. CH_4 gas flowed to the $CeNiO_3$-0.2G in the DRIFTS cell. The CH_4 peak was identified by a strong absorbance band at 3007 cm^{-1} and 1298 cm^{-1}, corresponding to the symmetric CH_4 bond. The gradual growth of the 2838 cm^{-1} band implies the dissociation of CH_4 on the Ni metal surface into CH_3^*. The band was accompanied by the slow growth of the 1860 cm^{-1} peak assigned to the C=O stretch. The results imply that CH_4 is

dissociated *via* multiple C–H dissociation steps on the metal surface, forming adsorbed carbon on Ni. The surface oxygen on CeO_2 might react with adsorbed carbon at the Ni/CeO$_2$ interface, forming adsorbed carbonate species. The suggestion was confirmed by the peak assigned to carbonate and bicarbonate in the 1742–1389 cm^{-1} region. The peak at 1742 cm^{-1} was also identified as a cerium oxycarbonate species ($Ce_2O_2CO_3$).[19] The peak at 2312 cm^{-1} implies the reaction of CH_4 with surface oxygen on the CeO_2, forming adsorbed $-CO_3$ species. The Ni surface is selective to CH_4 dissociation into atomic C. However, since CeO_2 has high oxygen mobility, it is clear from DRIFTS analysis that the adsorbed carbon reacts with surface oxygen to form adsorbed carbonate. However, the adsorbed carbonate is strongly attached to the surface, based on the increased intensity of such species with prolonged holding temperatures at 600 °C.

CO_2 adsorption on the catalysts was carried out at 600 °C. Note that the $CeNiO_3$ was treated again with a H_2 flow at 500 °C before CO_2 was introduced. The peak assigned to the absorbed *CO_2 gas phase was observed between 2500 and 2250 cm^{-1}. The small peak assigned to bidentate carbonate *bCO_3^{2-} was observed at 1743 and 1646 cm^{-1}. Additionally, the bidentate CO_3 peak was also observed at 1040 cm^{-1}. The peak at 1455 cm^{-1} refers to monodentate carbonate. The intensity of the bidentate carbonate band is higher than that of monodentate carbonate. The bicarbonate peak (HCO_3^-) was observed at 1425 cm^{-1}, implying the reaction of CO_2 with the surface OH^- species.

Different FTIR bands appeared after introducing mixed methane and carbon dioxide gases. The broad band at 2313 cm^{-1} is assigned to gaseous carbon dioxide, while the bands at 1306 cm^{-1}, 1336 cm^{-1} and 3010 cm^{-1} represent gaseous methane.[19] A negative methane peak at 3010 cm^{-1} was observed with increasing time at 600 °C, implying CH_4 decomposition during the DRM reaction. Monodentate carbonate and bidentate carbonate bands at 1455 cm^{-1} and 1510 cm^{-1} gained intensity in the presence of CH_4. The bicarbonate absorption band was also observed at 1643 cm^{-1}. A new species was observed at 2116 cm^{-1} assigned to CO formation. The peak at 1745 cm^{-1} was also identified as a cerium oxycarbonate species ($Ce_2O_2CO_3$).[19] The $Ce_2O_2CO_3$ species play a vital role as intermediates for removing the deposited carbon from the active metal during DRM. The formed Ce_2O_3 under reducing condition generates Ce^{3+} that reacted with CO_2 to form $Ce_2O_2CO_3$ species. The presence of Ce^{3+} was observed in XPS analysis. The lower intensity of $Ce_2O_2CO_3$ species in the $CH_4 + CO_2$ mixture compared to CH_4 gas only further evidenced the removal of deposited carbon from $CeNiO_3$. Another IR-band was observed at 2116 cm^{-1}, representing carbon monoxide formation during the reaction. These C–O bands begin to appear following CH_4 addition, which further supports the $Ce_2O_2CO_3$ species as vital intermediates for the oxidation of the dissociated oxygen atom from CO_2. Methane adsorption and dissociation occur at the surface of Ni active metal, while carbon dioxide adsorption and dissociation occur at the CeO_2 support. Carbon dioxide is absorbed on the oxygen vacancies of CeO_2 as bicarbonate species before undergoing oxygen dissociation to
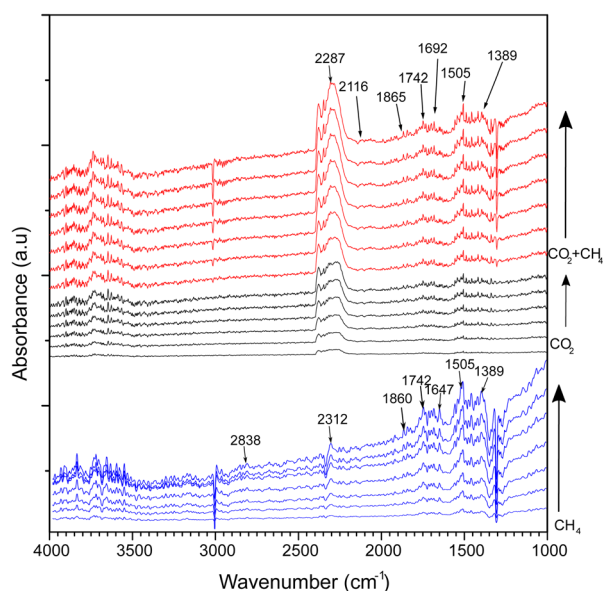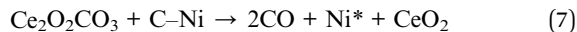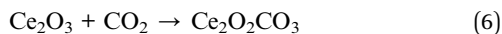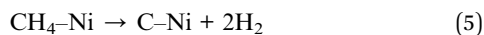

Fig. 9 *In situ* DRIFTS spectra of $CeNiO_3$ perovskite (0.2 g gelatin) under continuous flows of CH_4, CO_2 and a mixture of CO_2 and CH_4 at 600 °C.

form $Ce_2O_2CO_3$ species. The proposed mechanism for the reaction is given below.

$$CH_4 + Ni \rightarrow CH_4\text{--}Ni \qquad (4)$$

$$CH_4\text{--}Ni \rightarrow C\text{--}Ni + 2H_2 \qquad (5)$$

$$Ce_2O_3 + CO_2 \rightarrow Ce_2O_2CO_3 \qquad (6)$$

$$Ce_2O_2CO_3 + C\text{--}Ni \rightarrow 2CO + Ni^* + CeO_2 \qquad (7)$$

The difference in catalytic performance for $CeNiO_3$ catalysts synthesized using different gelatin concentrations might give insights into the structural properties of catalysts. In dry reforming of methane, CH_4 decomposed on the Ni via consecutive bond dissociation, producing adsorbed carbon species. CO_2 is absorbed on the CeO_2 surface, occupying surface oxygen vacancies that subsequently weaken the C–O bond. The dissociated oxygen migrated to the Ni/CeO_2 interface for the oxidation of adsorbed C as CO, while the CO leaves the CeO_2 surfaces. Strong CH_4 dissociation potential caused the conversion to deviate from the stoichiometric $CO_2 : CH_4$ ratio. As suggested by characterization data, the high dispersion of Ni on the CeO_2 surface, via either a high degree of NiO exsolution or the formation of uncoordinated Ni species, readily absorbs and dissociates CH_4 into H_2 gas. There is also a possibility that the generated H_2 reacts with the CO_2 reactant, producing CO through a reverse water gas shift reaction (eqn (2)). This step may be possible on $CeNiO_3$-0.1 G and $CeNiO_3$-0.05G because, despite similar CO_2 and CH_4 conversion, the H_2/CO ratio was less than 1. In the synthesis of $CeNiO_3$ perovskite, gelatin controlled the Ni^{2+} ion mobility in the cross-linked gel precursor. The Ni–gelatin complex inadvertently restricts the contact of Ni with the Ce^{2+} cation. At high gelatin concentrations, gelatin as a chelating agent might heavily saturate Ni^{2+}. The slow mobility of Ni^{2+} leads to the formation of uncoordinated Ni species, which causes deposition as NiO nanoparticles. The formation of uncoordinated NiO species alongside the main phase $CeNiO_3$ perovskite leads to a strong CH_4 dissociation site. Consequently, $CeNiO_3$-0.2G, obtained at high gelatin concentration, produced H_2/CO ratios >1.

Conclusion

Using gelatin at different concentrations to produce $CeNiO_3$ perovskite nanoparticles for dry reforming of methane significantly affects the stoichiometric H_2/CO formation. The preference for CH_4 decomposition on Ni metal surfaces was observed on $CeNiO_3$-0.2G due to the increase of the Ni surface area to 10 $m^2 g^{-1}$. Stoichiometric CH_4 and CO_2 conversion were achieved on $CeNiO_3$ obtained using low gelatin concentration (0.05 g and 0.1 g), suggesting that the exsolution of Ni from $CeNiO_3$ prevents fast methane decomposition. The expansion of the CeO_2 unit cells after the reaction suggests the exsolution of Ni from $CeNiO_3$ perovskite. Gelatin, as amine-based chelating agent, coordinates with Ni ions from the lone pair electrons on the nitrogen, forming octahedral binding. An optimized

chelating agent amount is essential for forming stable metal ion bonds. Gelatin reduced Ni mobility in the cross-linked gel precursor, restricting the contact between the cations. Therefore, gelatin facilitates uniformity in the particle size distribution and forms smaller particles. However, at higher gelatin concentrations, the reduced Ni mobility may restrict the self-assembly of $CeNiO_3$ perovskite. $CeNiO_3$ perovskite shows catalytic stability at 600 °C with a H_2/CO ratio of ~8.5 when produced using low gelatin amounts (0.05 g and 0.1 g).

Experimental

Materials

Cerium nitrate hexahydrate ($Ce(NO_3)_3 \cdot 6H_2O$, Merck, >99%), nickel nitrate hexahydrate ($Ni(NO_3)_2 \cdot 6H_2O$, Merck, >99%), gelatin (bovine skin type B, Sigma Aldrich) and distilled water were directly used without further purification.

Catalyst preparation

The synthesis of $CeNiO_3$ was conducted based on previous studies with slight modifications.[23] The amount of gelatin was varied to obtain the weight ratios of gelatin to the final product of 1 : 0.01 (0.05 g gelatin), 1 : 0.03 (0.1 g gelatin) and 1 : 0.06 (0.2 g gelatin). Gelatin was used as a chelating agent for Ni to synthesize $CeNiO_3$ perovskites.[58] Gelatin was dissolved in distilled water (30 g) and stirred at 50 °C for 30 min to obtain a clear solution. Equimolar solutions of metal nitrates such as $Ce(NO_3)_2 \cdot 6H_2O$ and $Ni(NO_3)_2 \cdot 6H_2O$ were added to the solution and stirred at 70 °C. The solution temperature was raised to 90 °C using a hot plate and stirring until the solution turned into a gel. The gel was heated in a muffle furnace with double calcination. Firstly, the gel was calcined at 350 °C for 2 hours to obtain a dried powder. This powder was ground and calcined at 900 °C for 4 hours at a ramping rate of 5 °C min^{-1}. The purpose of double calcination is to remove the impurities to form a high purity product.

Characterization

The properties of the perovskite were investigated using a Shimadzu XRD-7000 with Cu Kα 1.5418 Å radiation. The scan rate was 5° min^{-1} in the 2θ range of 10°–90° and the crystal structure was analyzed using X'Pert High Score Plus software. The lattice parameters are calculated using eqn (8),

$$a = \frac{\lambda}{2 \sin \theta} \sqrt{h^2 + k^2 + l^2} \qquad (8)$$

where λ is the Cu Kα wavelength, θ is the Bragg angle, and hkl is Miller's index.

H_2-TPR analyses were performed using a ChemBET Pulsar TPR/TPD equipped with a thermal conductivity detector. H_2-TPR analyses involve the activation of the catalyst with H_2 at a high temperature of 900 °C with a ramping rate of 10 °C min^{-1}. A very small amount of samples, i.e. 20 mg, was placed in a U-shaped tube. The textural properties of perovskites were measured using N_2-physisorption using a Micromeritics ASAP2020 instrument at 77 K. The Brunauer–Emmett–Teller

(BET) method was employed to determine the surface area of the catalyst, while the pore diameter of the catalyst was determined by applying the Barrett–Joyner–Halenda (BJH) method using nitrogen isotherms. X-ray photoelectron spectroscopy (XPS) analysis was performed using a Kratos Axis Ultra-DLD XPS spectrometer with a monochromatic Al Kα source (75–150 W) and an analyzer pass energy of 160 eV for survey scans or 40 eV for detailed scans. High-resolution transmission electron microscopy (Tecnai G2 20S) determined the nanostructure and surface morphology. Raman spectra were recorded using a Scanner 5.0 Raman system assembled at National Taiwan University with a 532 nm wavelength laser.

Catalytic dry reforming reaction

The catalytic activity of $CeNiO_3$ was determined in a tubular fixed bed quartz reactor with a 4 mm internal diameter and 40 cm length. $CeNiO_3$ was reduced *in situ* with pure hydrogen at 20 mL min^{-1} at 500 °C for 3 hours before the reaction. The H_2 gas was switched to a mixed gas containing 25% CO_2 and 25% CH_4 in nitrogen at 20 mL min^{-1} after the furnace reached room temperature. The flow rates of gases were controlled using calibrated mass flow controllers (MFCs). Online gas chromatography (GC), which is equipped with thermal conductivity (TCD) and flame ionizing (FID) detectors, was used for the analysis of the reaction mixture.

The conversion of the reactants was calculated using the following formula:

$$X_{CH_4} = \frac{P_{CH_4,in} - P_{CH_4,out}}{P_{CH_4,in}} \times 100\% \qquad (9)$$

$$X_{CO_2} = \frac{P_{CO_2,in} - P_{CO_2,out}}{P_{CO_2,in}} \times 100\% \qquad (10)$$

where X_{CH_4} represent the % conversion of CH_4, X_{CO_2} represents the % conversion of CO_2, $P_{CH_4,in}$ and $P_{CH_4,out}$ are the peak areas of CH_4 before and after the reaction, and $P_{CO_2,in}$ and $P_{CO_2,out}$ are the peak areas of CO_2 before and after the reaction.

Conclusions

Using gelatin at different concentrations to produce $CeNiO_3$ perovskite nanoparticles for dry reforming of methane has a significant effect on stoichiometric H_2/CO formation. The preference for CH_4 decomposition on Ni metal surfaces was observed on $CeNiO_3$-0.2G due to the increase of the Ni surface area. Stoichiometric CH_4 and CO_2 conversion was achieved on $CeNiO_3$ obtained using low gelatin concentration (0.05 g and 0.1 g), which suggests that control exsolution of Ni from $CeNiO_3$ prevents fast methane decomposition. The shift of the CeO_2 (111) plane to lower 2θ after the reaction suggests the exsolution of Ni from $CeNiO_3$-0.05G perovskite. Meanwhile, $CeNiO_3$-0.2G shows a similar peak position, suggesting that NiO was deposited on CeO_2 at high gelatin concentration, instead of being incorporated into $CeNiO_3$ perovskite. Gelatin as an amine based chelating agent coordinates with Ni ions from the lone pair of electrons on the nitrogen, forming octahedral binding. An optimized chelating agent amount is essential to form stable bonds of metal ions. Gelatin reduced Ni mobility in the cross-linked gel precursor, restricting the contact between the Ni and Ce cations. Therefore, gelatin facilitates uniformity in the particle size distribution and forms smaller particles. However, at higher gelatin concentrations, the reduced Ni mobility may restrict the self-assembly of $CeNiO_3$ perovskite. $CeNiO_3$ perovskite shows catalytic stability at 600 °C with a H_2/CO ratio close of 0.85 when produced using low gelatin amounts (0.05 g and 0.1 g).

Data availability

The data supporting this article have been included as part of the ESI.†

Conflicts of interest

There are no conflicts to declare.

Acknowledgements

References

1 T. Abbasi, M. Premalatha and S. A. Abbasi, *Renewable Sustainable Energy Rev.*, 2011, **15**, 891–894.

2 C.-F. Schleussner, J. Rogelj, M. Schaeffer, T. Lissner, R. Licker, E. M. Fischer, R. Knutti, A. Levermann, K. Frieler and W. Hare, *Nat. Clim. Change*, 2016, **6**, 827–835.

3 J. Rogelj, M. Den Elzen, N. Höhne, T. Fransen, H. Fekete, H. Winkler, R. Schaeffer, F. Sha, K. Riahi and M. Meinshausen, *Nature*, 2016, **534**, 631–639.

4 J. Hansen, R. Ruedy, M. Sato and K. Lo, *Rev. Geophys.*, 2010, **48**, RG4004.

5 J. Szczygieł, K. Chojnacka, D. Skrzypczak, G. Izydorczyk, K. Moustakas and M. Kułażyński, *J. Environ. Manage.*, 2023, **325**, 116463.

6 F. G. M. de Medeiros, F. W. B. Lopes and B. Rego de Vasconcelos, *Catalysts*, 2022, **12**, 363.

7 B. C. Ekeoma, M. Yusuf, K. Johari and B. Abdullah, *Int. J. Hydrogen Energy*, 2022, 41596–41620.

8 E. Le Saché and T. R. Reina, *Prog. Energy Combust. Sci.*, 2022, **89**, 100970.

9 T. Ban, X.-Y. Yu, H.-Z. Kang, H.-X. Zhang, X. Gao, Z.-Q. Huang and C.-R. Chang, *J. Catal.*, 2022, **408**, 206–215.

10 Z. Li, Z. Wang and S. Kawi, *ChemCatChem*, 2019, **11**, 202–224.

11 S. Bhattar, M. A. Abedin, S. Kanitkar and J. J. Spivey, *Catal. Today*, 2021, **365**, 2–23.

12 N. Ahmad, R. Wahab, S. Manoharadas, B. F. Alrayes, M. Alam and F. A. Alharthi, *Molecules*, 2022, **27**, 356.

13 G. Valderrama, A. Kiennemann, C. U. de Navarro and M. R. Goldwasser, *Appl. Catal., A*, 2018, **565**, 26–33.

14 M. Tyunina, J. Levoska, O. Pacherova, T. Kocourek and A. Dejneka, *J. Mater. Chem. C*, 2022, **10**, 6770–6777.

15 N. Ahmad, F. Alharthi, M. Alam, R. Wahab, S. Manoharadas and B. Alrayes, *Energies*, 2021, **14**, 2928.

16 D. Navas, S. Fuentes, A. Castro-Alvarez and E. Chavez-Angel, *Gels*, 2021, **7**, 275.

17 Z. Mhlwatika, R. Meijboom and N. Bingwa, *Inorg. Chem. Commun.*, 2021, **133**, 108962.

18 A. E. Abasaeed, M. L. Sofiu, K. Acharya, A. I. Osman, A. H. Fakeeha, R. L. AL-Otaibi, A. A. Ibrahim, A. S. Al-Awadi, H. Bayahia, S. A. Al-Zahrani, R. Kumar and A. S. Al-Fatesh, *Energy Sci. Eng.*, 2023, **11**, 1436–1450.

19 Z. Du, C. Petru, X. Yang, F. Chen, S. Fang, F. Pan, Y. Gang, H.-C. Zhou, Y. H. Hu and Y. Li, *J. CO$_2$ Util.*, 2023, **67**, 102317.

20 B. G. Kim, W. Jang, Y. J. Park, J. H. Kang, J. H. Seo and D. H. Wang, *J. Phys. Chem. C*, 2020, **124**, 25184–25195.

21 M. Awais, S. Kundu, D. Zhang, V. Yeddu, M. R. Kokaba, Y. Ahmed, W. Zhou, S. Dayneko, F. Tan and M. I. Saidaminov, *Cell Rep. Phys. Sci.*, 2023, **4**, 101634.

22 Q. A. Islam, S. Paydar, N. Akbar, B. Zhu and Y. Wu, *J. Power Sources*, 2021, **492**, 229626.

23 N. Azad, H. Arabi, S. R. Ghorbani and A. Davodi, *J. Sol-Gel Sci. Technol.*, 2018, **88**, 465–473.

24 G. Monros, J. Cards, M. A. Tena, P. Escribano, J. Badenes and E. Cordoncillo, *J. Mater. Chem.*, 1995, **5**, 85–90.

25 F. Dehghani, S. Ayatollahi, S. Bahadorikhalili and M. Esmaeilpour, *Pet. Chem.*, 2020, **60**, 731–743.

26 M. Harikrishnan, A. J. C. Mary and A. C. Bose, *Electrochim. Acta*, 2020, **362**, 137095.

27 J. Chen, Z. He, G. Li, T. An, H. Shi and Y. Li, *Appl. Catal., B*, 2017, **209**, 146–154.

28 S. Mahammadunnisa, P. M. K. Reddy, N. Lingaiah and C. Subrahmanyam, *Catal. Sci. Technol.*, 2013, **3**, 730–736.

29 H. Chen, C. Lim, M. Zhou, Z. He, X. Sun, X. Li, Y. Ye, T. Tan, H. Zhang, C. Yang, J. W. Han and Y. Chen, *Advanced Science*, 2021, **8**, 2102713.

30 Z. Yang, D. Zheng, X. Yue, K. Wang, Y. Hou, W. Dai and X. Fu, *Appl. Surf. Sci.*, 2023, **615**, 156311.

31 J. Kojčinović, D. Tatar, S. Šarić, C. B. Pravda, A. Mavrič, I. Arčon, Z. Jagličić, M. Mellin, M. Einert, A. Altomare, R. Caliandro, Á. Kukovecz, J. P. Hofmann and I. Djerdj, *Dalton Trans.*, 2024, **53**, 2082–2097.

32 S. Loridant, *Catal. Today*, 2021, **373**, 98–111.

33 J. E. Spanier, R. D. Robinson, F. Zhang, S.-W. Chan and I. P. Herman, *J. Appl. Phys.*, 2001, **64**, 245407.

34 I. Kosacki, T. Suzuki, H. U. Anderson and P. Colomban, *Solid State Ionics*, 2002, **149**, 99–105.

35 C. C. Yang and S. Li, *J. Phys. Chem. B*, 2008, **112**, 14193–14197.

36 Z. Popović, Z. Dohčević-Mitrović, N. Paunović and M. Radović, *Phys. Rev. B: Condens. Matter Mater. Phys.*, 2012, **85**, 014302.

37 J. R. McBride, K. C. Hass, B. D. Poindexter and W. H. Weber, *J. Appl. Phys.*, 1994, **76**, 2435–2441.

38 Y. Li, Z. Wei, F. Gao, L. Kovarik, R. A. L. Baylon, C. H. F. Peden and Y. Wang, *ACS Catal.*, 2015, **5**, 3006–3012.

39 T. Taniguchi, T. Watanabe, N. Sugiyama, A. K. Subramani, H. Wagata, N. Matsushita and M. Yoshimura, *J. Phys. Chem. C*, 2009, **113**, 19789–19793.

40 D. B. Long, B. T. Hau, N. T. T. Van, N. P. Anh, T. G.-T. Ho, H. C. Anh, P. H. Phuong, C. D. Huy, N. Tri and L. C. Loc, *J. Sci.: Adv. Mater. Devices*, 2023, **8**, 100610.

41 B. M. Al-Swai, N. Osman, M. S. Alnarabiji, A. A. Adesina and B. Abdullah, *Ind. Eng. Chem. Res.*, 2018, **58**, 539–552.

42 B. Kitiyanan, W. E. Alvarez, J. H. Harwell and D. E. Resasco, *Chem. Phys. Lett.*, 2000, **317**, 497–503.

43 Y. Feng, G. Zhou, G. Wang, M. Qu and Z. Yu, *Chem. Phys. Lett.*, 2003, **375**, 645–648.

44 O. Omoregbe, H. T. Danh, S. Z. Abidin, H. D. Setiabudi, B. Abdullah, K. B. Vu and D.-V. N. Vo, *Procedia Eng.*, 2016, **148**, 1388–1395.

45 N. Tri, N. P. Anh, T. D. Huy, D. B. Long, H. C. Anh, P. H. Phuong, N. T. T. Van, T.-T. Nguyen and L. C. Loc, *J. Sci.: Adv. Mater. Devices*, 2023, **8**, 100529.

46 M. B. Islam, M. Yanagida, Y. Shirai, Y. Nabetani and K. Miyano, *ACS Omega*, 2017, **2**, 2291–2299.

47 D. S. Mann, S.-N. Kwon, P. Patil and S.-I. Na, *Nano Energy*, 2023, **106**, 108062.

48 C. C. Boyd, R. C. Shallcross, T. Moot, R. Kerner, L. Bertoluzzi, A. Onno, S. Kavadiya, C. Chosy, E. J. Wolf, J. Werner, J. A. Raiford, C. de Paula, A. F. Palmstrom, Z. J. Yu, J. J. Berry, S. F. Bent, Z. C. Holman, J. M. Luther, E. L. Ratcliff, N. R. Armstrong and M. D. McGehee, *Joule*, 2020, **4**, 1759–1775.

49 M. C. Biesinger, B. P. Payne, A. P. Grosvenor, L. W. Lau, A. R. Gerson and R. S. C. Smart, *Appl. Surf. Sci.*, 2011, **257**, 2717–2730.

50 X. Wang, B. Zhang, W. Zhang, M. Yu, L. Cui, X. Cao and J. Liu, *Sci. Rep.*, 2017, **7**, 1584.

51 E. Y. Konysheva and S. M. Francis, *Appl. Surf. Sci.*, 2013, **268**, 278–287.

52 F. Rao, Y. An, G. Zhu, S. Gong, L. Zhu, H. Lu, X. Shi, Y. Huang, F. Zhang and M. Hojamberdiev, *Sep. Purif. Technol.*, 2024, **333**, 125951.

53 I. Bertóti, M. Mohai and K. László, *Carbon*, 2015, **84**, 185–196.

54 G. Greczynski and L. Hultman, *Sci. Rep.*, 2021, **11**, 11195.

55 X. Chen, X. Wang and D. Fang, *Fullerenes, Nanotubes Carbon Nanostruct.*, 2020, **28**, 1048–1058.

56 A. Manakhov, P. Kiryukhantsev-Korneev, M. Michlíček, E. Permyakova, E. Dvořáková, J. Polčák, Z. Popov, M. Visotin and D. V. Shtansky, *Appl. Surf. Sci.*, 2018, **435**, 1220–1227.

57 Y. Liu, H. Yan, X. Chen, X. Feng and C. Yang, *J. Anal. Appl. Pyrolysis*, 2019, **141**, 104629.

58 F. S. Oliveira, P. M. Pimentel, D. M. d. A. Melo, R. M. P. B. Oliveira, M. A. d. F. Melo and O. R. Bagnato, Synthesis of Sm_1_-_xSr_xNiO"3 systems for application in dry reforming reaction, *PTECH 2009: 7 International latin-american conference on powder technology*, Brazil, 2009.